Kinematic and deformation parameter measurement by spatiotemporal analysis of an interferogram sequence

Groves, Roger M.; Fu, Yu; Pedrini, Giancarlo; Osten, Wolfgang

2007

Fu, Y., Groves, R. M., Pedrini, G., & Osten, W. (2007). Kinematic and deformation parameter measurement by spatiotemporal analysis of an interferogram sequence. Applied Optics, 46(36), 8645-8655.

https://hdl.handle.net/10356/92038

https://doi.org/10.1364/AO.46.008645

Kinematic and deformation parameter measurement by spatiotemporal analysis of an interferogram sequence

Yu Fu,[1,2,*] Roger M. Groves,[1] Giancarlo Pedrini,[1] and Wolfgang Osten[1]

[1]Institut für Technische Optik, Universität Stuttgart, Pfaffenwaldring 9, D-70569 Stuttgart, Germany
[2]Department of Mechanical Engineering, National University of Singapore, 10 Kent Ridge Crescent, Singapore 119260

*Corresponding author: fuyu@ito.uni-stuttgart.de

Received 4 September 2007; revised 7 November 2007; accepted 15 November 2007;
posted 16 November 2007 (Doc. ID 87220); published 19 December 2007

In recent years, optical interferometry has been applied to the whole-field, noncontact measurement of vibrating or continuously deforming objects. In many cases, a high resolution measurement of kinematic (displacement, velocity, and acceleration, etc.) and deformation parameters (strain, curvature, and twist, etc.) can give useful information on the dynamic response of the objects concerned. Different signal processing algorithms are applied to two types of interferogram sequences, which were captured by a high-speed camera using different interferometric setups: (1) a speckle or fringe pattern sequence with a temporal carrier and (2) a wrapped phase map sequence. These algorithms include Fourier transform, windowed Fourier transform, wavelet transform, and even a combination of two of these techniques. We will compare these algorithms using the example of a 1D temporal evaluation of interferogram sequences and extend these algorithms to 2D and 3D processing, so that accurate kinematic and deformation parameters of moving objects can be evaluated with different types of optical interferometry.

OCIS codes: 120.5050, 100.7410, 100.6890, 090.2880, 120.7280.

1. Introduction

Optical interferometric techniques such as geometric moiré, holography, moiré interferometry, and shearography have been developed for the measurement of a wide range of physical parameters, such as displacement, strain, surface profile, and refractive index. They have advantages over other techniques as they are noncontacting and they provide whole-field information. Due to the rapid development of computer and imaging sensor technology, most optical interferometric techniques have their digital version, for example, electronic speckle interferometry (ESPI), digital speckle shearing interferometry (DSSI), and digital holography. The results obtained by the aforesaid methods are usually in the form of speckle or fringe patterns. For accurate mapping of the interference phase, various image processing algorithms, notably carrier-based spatial Fourier transform (FT) [1] and phase shifting [2], have been used.

Since the 1960s, optical interferometry has been applied to the whole-field, noncontact dynamic measurement [3]. For high-frequency vibration, optical interferometry is normally applied to determine vibration modes of objects [4]. Time-average methods, based on holography, ESPI, DSSI, or moiré, possess many advantages over the other techniques. They directly acquire a spatially dense, full-field, real-time image of the mode shape, while other techniques require the reconstruction of the mode shape from single point measurements. In addition, there is no physical contact between the sensor and the structure in optical techniques, thus eliminating the disturbing influences of mass loading and local stiffening changes associated with contact sensors. However, the time-average method is not suitable for measuring the transient deformation of a continuously deforming object or a vibrating object. The use of a twin-cavity double-pulsed laser in the interferometry [5–7] has been reported as an alternative to obtain these transient deformations. Unfortu-

0003-6935/07/368645-11$15.00/0

nately, this technique has an important limitation. To obtain the evolution of the transient deformation, an experiment must be repeated many times with a different interval of two pulses. This means nonrepeatable events cannot be studied in detail.

With the availability of high-speed digital recording and powerful lasers, it is now possible to record interferograms with rates exceeding 100,000 frames per second (fps) [8]. Sometimes these interferograms are preprocessed to a sequence of wrapped 2D phase maps by different techniques, such as a carrier-based 2D Fourier analysis [1] or a reconstruction of a digital hologram sequence [9]. Normally these wrapped phase maps are noisy and are not suitable for spatial phase unwrapping. In the 1990s, a new phase evaluation method based on temporal analysis [10,11] was introduced. It analyzes the phase point by point along the time axis, so that the speckle noise in adjacent pixels does not affect the measurement. In addition, it expands the displacement measurement range to more than 500 μm [12]. A FT [13] is usually applied to extract the phase in the temporal domain. In recent years, wavelet analysis [14,15] has also been introduced for temporal phase extraction. It can eliminate the influence of various noise sources and improve the measurement result. Furthermore, it can also extract the instantaneous frequency of the temporal intensity variation from which the velocity of the deformation can be evaluated. However, a systematic error is found in phase extraction by continuous wavelet transform (WT) when the signal frequency is varying [16].

The temporal phase analysis technique has its own disadvantage. When the intensity variations of pixels are analyzed, it cannot extract the phase from a part of an object that is not moving with the rest or from objects that deform in different directions at different parts. Without a temporal carrier [13,17] neither Fourier analysis nor wavelet analysis allows the determination of the absolute sign of the phase. This limits the technique to the measurement of deformation in one known direction. Similar to a spatial carrier, a temporal carrier can also be introduced in the image acquisition process to overcome these problems, at the cost of a reduced measurement range of phase variation.

In a dynamic measurement, the instantaneous displacement is not the only key parameter of interest. Other instantaneous kinematic and deformation parameters are sometimes more important in studying the mechanical behavior of a continuously deforming or vibrating object. For example, the curvature and twist, the second-order derivatives of out-of-plane displacement along the spatial axis, are directly related to the flexural and torsional movements, respectively [18,19].

The definitions of parameters included in this paper are: (1) displacement Z is the distance moved since the first frame of the measurement process. Different optical techniques and configurations will yield interferograms representing the displacement in different directions. However, in this investigation, only the out-of-plane displacement is studied, and all the examples illustrated in this paper are as such. (2) Velocity $v_Z = \mathrm{d}Z/\mathrm{d}t$ is the first-order derivative of displacement along the time axis. (3) Acceleration $a_Z = \mathrm{d}^2Z/\mathrm{d}t^2$ is the second-order derivative of displacement along the time axis. (4) w is a relative out-of-plane displacement, referenced to a fixed point on the object surface. It is possible to evaluate this displacement through spatial phase analysis. (5) Surface strains ($\partial w/\partial x$ and $\partial w/\partial y$) are the first-order derivatives of the deformation along the spatial axis. (6) Curvature ($\partial^2 w/\partial x^2$ and $\partial^2 w/\partial y^2$) and twist ($\partial^2 w/\partial x \partial y$) are the second-order derivatives of deformation along the spatial axis.

The purpose of this investigation is to evaluate the above-mentioned parameters from an interferogram sequence captured by a high-speed camera of continuously deforming and vibrating objects. Our investigation will start with a 1D temporal analysis using three different signal processing techniques: FT, windowed Fourier transform (WFT) [19–21], and complex Morlet WT [22–24]. A simulated 1D temporal signal will be processed by different techniques, and the advantages and disadvantages of each technique will be illustrated. A new method based on the combination of FT and WFT will be proposed for the temporal analysis, in order to eliminate the noise effect and to evaluate the kinematic parameters more accurately. An example of a displacement, a velocity, and an acceleration evaluation on a vibrating earphone membrane by digital holography will be presented. Then the process will be extended to the 2D spatial [25] and 3D spatiotemporal [26] cases, so that the deformation parameters can also be evaluated. Simulation results in the 2D case will be given in order to illustrate the accuracy for deformation parameter measurement, and an ESPI experiment result on a continuously deforming plate will also show the performance of the proposed method on the kinematic and deformation parameter evaluation from an interferogram sequence.

2. Principles

In high-speed optical dynamic measurement, a sequence of interferograms is captured by a high-speed camera. These interferograms could be a sequence of original speckle or fringe patterns, or a sequence of wrapped phase map after preprocessing. The preprocessing could be a reconstruction of a digital hologram, a high-speed phase-stepping processing, or a carrier-based Fourier analysis. Processing of these 3D intensity or wrapped phase matrices enables the measurement of kinematic and deformation parameters of the object. A 1D temporal process on each pixel is usually the first step of the analysis.

In this paper, the temporal signals on each pixel are classified into two types: (I) intensity variation with a known uniform direction of phase change, and (II) exponential phase signal. The first type of signal on point $P(x, y)$ can be written as

$$f_{\mathrm{I}}(x, y; t) = I_b(x, y; t) + A(x, y; t)\cos(\varphi(x, y; t)), \quad (1)$$

where $I_b(x, y; t)$ and $A(x, y; t)$ are the intensity bias and the modulation factor, respectively. These two items are both slowly varying functions along the time axis. $\varphi(x, y; t) = \varphi_C(t) + \varphi_O(x, y; t)$ is a single-directional phase variation of the signal of each pixel. In ESPI, it can be obtained for a continuously deforming object, where all points are deforming in a known direction or on a vibrating object with a temporal carrier. $\varphi_C(t)$ is the phase change due to the temporal carrier; it is normally uniform for each pixel. $\varphi_O(x, y; t)$ is the phase variation due to a vibration or displacement with an unknown direction. The temporal carrier frequency should be high enough that the phase change at each pixel is only in one direction. In addition, the signal frequency component should be separable from the zero-frequency components, but should be able to be sampled according to the Nyquist theorem. In general, the introduction of a temporal carrier will reduce the measurement range of deformation velocity.

The second type of temporal signal is the exponential phase signal,

$$f_{II}(x, y; t) = \exp(j\phi(x, y; t)), \tag{2}$$

where $j = \sqrt{-1}$ and $\phi(x, y; t)$ is the phase value on point $P(x, y)$ at instant t. It is worth noting that the phase ambiguity problem mentioned above does not exist in the exponential phase signal. The phase variation could be in both directions, and no temporal carrier is needed. However, a carrier is still necessary for obtaining the phase signal itself, either by standard FT or dynamic phase shifting [27,28]. This carrier also exists in digital holography, arising from the small angle between object and reference beams. In this investigation, these two types of signals are processed by following different signal processing techniques.

A. Fourier Transform

FT and inverse FT are widely used in signal processing and phase extraction. The FT of a 1D temporal signal $f(t)$ and its inverse FT can be expressed, respectively, as

$$\hat{f}(\xi) = \int_{-\infty}^{+\infty} f(t)\exp(-j\xi t)\mathrm{d}t, \tag{3}$$

$$f(t) = \frac{1}{2\pi}\int_{-\infty}^{+\infty} \hat{f}(\xi)\exp(j\xi t)\mathrm{d}\xi, \tag{4}$$

where $\hat{f}(\xi)$ is the FT of $f(t)$. When $f(t)$ is the first type of temporal signal given by Eq. (1), the Fourier spectrum of $f(t)$ will be

$$\hat{f}(\xi) = DC(\xi) + \hat{C}(\xi) + \hat{C}^*(\xi), \tag{5}$$

where the asterisk denotes the complex conjugate. $DC(\xi)$ represents the contribution to the spectra from low-frequency background illumination and it is centered around the zero-order term $\xi = 0$, $\hat{C}(\xi)$ and $\hat{C}^*(\xi)$ are centered around $\xi = \xi_C$ and $\xi = -\xi_C$, where ξ_C is the temporal carrier frequency. $DC(\xi)$ and $\hat{C}^*(\xi)$ can be eliminated by bandpass filtering. The inverse FT of $\hat{C}(\xi)$ yields an exponential signal $C(t)$ from which the phase can be calculated by

$$\varphi(t) = \arctan\frac{\mathrm{Im}(C(t))}{\mathrm{Re}(C(t))}, \tag{6}$$

where Im and Re denote the imaginary and real parts of $C(t)$, respectively. The phase obtained is wrapped between $-\pi$ to $+\pi$. A 1D temporal unwrapping procedure is needed to reconstruct the continuous phase function $\varphi(t)$. A similar process can be applied when $f(t)$ is an exponential signal, as shown in Eq. (2). The spectrum of an exponential signal could be in both positive and negative frequency areas, but with the $DC(\xi)$ and the conjugate terms absent.

It is well known that the accuracy of a FT analysis increases with the decrease of the width of the spectrum. However, when the phase change of the signal is highly nonlinear, the width of the sideband in the spectrum increases. This occurs quite often in dynamic measurements as the velocity of the object normally varies. In addition, different pixels have different spectra. The selection of a proper window for bandpass filtering for all pixels becomes difficult. Normally the maximum and minimum frequencies of all pixels are evaluated before processing, and a relatively large filtering window size is determined accordingly. This means that noise whose frequency is within the filtering windows cannot be removed by FT. This problem can be overcome by using a WFT.

B. Windowed Fourier Transform

A 1D WFT of a temporal signal $f(t)$ and its inverse windowed Fourier transform (IWFT) can be written as [29]:

$$Sf(u, \xi) = \int_{-\infty}^{+\infty} f(t)g_{u,\xi}^*(t)\mathrm{d}t, \tag{7}$$

$$f(t) = \frac{1}{2\pi}\int_{-\infty}^{+\infty}\int_{-\infty}^{+\infty} Sf(u, \xi)g_{u,\xi}(t)\mathrm{d}\xi\mathrm{d}u, \tag{8}$$

where $Sf(u, \xi)$ denotes the spectrum of WFT and $g_{u,\xi}(t)$ is the WFT kernel, which can be expressed as

$$g_{u,\xi}(t) = g(t - u)\exp(j\xi t). \tag{9}$$

The window $g(t)$ is usually chosen as the Gaussian function:

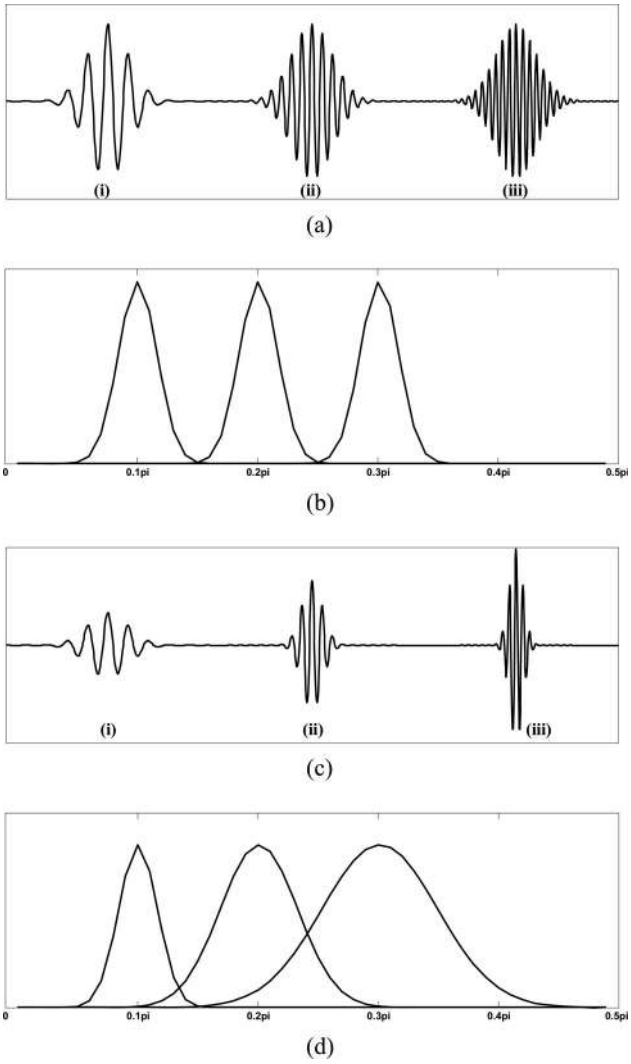

Fig. 1. (a) Real part of a windowed Fourier kernel at different frequencies: 0.1π, 0.2π, and 0.3π. The window size is set as $\sigma = 20$. (b) Spectrum of windowed Fourier kernels in (a). (c) Real part of a complex Morlet wavelet at different frequencies: 0.1π, 0.2π, and 0.3π ($a = 20$, 10, and 6.67). (d) Spectrum of complex Morlet wavelets in (c).

$$g(t) = \exp(-t^2/2\sigma^2), \tag{10}$$

which permits the best time-frequency localization in analysis. σ is a parameter to control the expansion of the window size. Figure 1(a) shows the real part of a windowed Fourier kernel at different frequencies: 0.1π, 0.2π, and 0.3π when $\sigma = 20$. Their spectra are shown in Fig. 1(b). It can be observed that the window size remains the same at different frequencies.

When the signal processed by WFT is an exponential phase signal f_{II}, the WFT can be expressed as [29],

$$Sf_{\mathrm{II}}(u, \xi) = \frac{\sqrt{s}}{2} A(u)\exp(j[\varphi(u) - \xi u])(\hat{g}(s[\xi - \varphi'(u)]) + \varepsilon(u, \xi)), \tag{11}$$

where u and ξ represent the time and frequency, respectively and s is a scaling factor. For a fixed s, $g_s(t) = s^{-1/2}g(t/s)$ has a support size of s. $A(u)$ is the modulus of f_{II} [in this case, $A(u) = 1$] and $\varepsilon(u, \xi)$ is a corrective term, which can be neglected if $A(u)$ and $\varphi'(u)$ have small relative variations over the support of window g. $\hat{g}(\omega)$ denotes the FT of $g(t)$. The trajectory of the maximum $|Sf_{\mathrm{II}}(u, \xi)|^2$ on the plane is called a windowed Fourier "ridge." Since $|\hat{g}(\omega)|$ is a maximum at $\omega = 0$, and if ε is negligible, $|Sf_{\mathrm{II}}(u, \xi)|^2$ reaches a maximum when

$$\xi(u) = \varphi'(u), \tag{12}$$

where $\varphi'(u)$ is defined as the instantaneous frequency of the signal, which is proportional to the velocity of the point $P(x, y)$. A filtered signal phase can be obtained by integration. For an intensity varying signal f_{I}, the direct use of a WFT may generate a large error, due to the effect of the *DC* term and even the negative frequency. This problem will be illustrated with a simulated signal in Subsection 3.

A WFT maps a 1D temporal signal to a 2D time-frequency plane and extracts the signal's instantaneous frequency. Thus it is more effective to remove the noise within the frequency band of the signal. This is the advantage of the WFT over FT. However, the time-frequency uncertainty principle affects the resolution, which leads to a trade-off between time and frequency localization. The narrower the time window, the better the temporal resolution at the cost of a poorer resolution in frequency and vice versa. However, once the window size is determined, WFT has a uniform resolution at different frequencies. In many cases, a high-frequency resolution is needed when the signal frequency is low, and a low-frequency resolution can be accepted when the signal frequency is high. This leads to another signal processing algorithm, the WT.

C. Wavelet Transform

WT is similar to WFT, but with a varying window size according to the signal frequency. A WT of an intensity varying signal f_{I} can be expressed as

$$Wf(a, b) = \frac{1}{\sqrt{a}}\int_{-\infty}^{+\infty} f(t)\Psi^*\left(\frac{t-b}{a}\right)\mathrm{d}t = \frac{1}{\sqrt{a}}\int_{-\infty}^{+\infty} f(t)\Psi_{ab}{}^*(t)\mathrm{d}t, \tag{13}$$

where $\Psi(t)$ is known as the mother wavelet and $\Psi_{ab}(t)$ are the basis functions of the transform, known as daughter wavelets. a is the scaling factor related to the frequency, and b is the time shift. While similar to the WFT mentioned above, it is more appropriate to use a complex function as the mother wavelet, in order to properly separate the phase and amplitude information of the signal. The most commonly used mother wavelet for such an application is the complex Morlet wavelet, which is the product of a real Gauss-

ian window and a complex oscillating exponential function,

$$\Psi(t) = g(t)\exp(i\omega_0 t), \tag{14}$$

where $g(t) = \exp(-(t^2/2))$. ω_0 is the "mother" frequency or central frequency, and this is the only parameter that has to be selected. The different wavelets used during time-frequency analysis are derived from the mother wavelet by scaling a and time shift b. Hence, a wavelet derived from the mother wavelet takes the form:

$$\Psi_{ab}(t) = \Psi\left(\frac{t-b}{a}\right) = \exp\left(-\frac{(t-b)^2}{2a^2}\right)\exp\left(i\,\frac{\omega_0}{a}(t-b)\right). \tag{15}$$

To satisfy the admissibility condition, ω_0 must be larger than 5 [23]. A proper selection of the central frequency ω_0 determines the overall "balance" between time and frequency resolution. In this study, ω_0 is selected as 2π to satisfy the admissibility condition and to keep the flexibility of the wavelet analysis. The relationship between frequency ξ and the scaling factor a is given by

$$\xi = \frac{\omega_0}{a} = \frac{2\pi}{a}. \tag{16}$$

Figure 1(c) shows the real part of a complex Morlet wavelet at different frequencies: 0.1π, 0.2π, and 0.3π ($a = 20$, 10, and 6.67). Their spectra are shown in Fig. 1(d). It can be observed that the extent of the analysis window in the WT varies according to the analysis frequency ξ. The wavelet coefficient can be written as [29],

$$Wf(a,\,b) = \frac{\sqrt{a}}{2}A(b)\{\hat{g}[a(\xi - \varphi'(b))] + \varepsilon(b,\,\xi)\}\exp[i\varphi(b)], \tag{17}$$

where $\varepsilon(b, \xi)$ is a corrective term which is negligible if the conditions $[\omega_0{}^2/|\varphi'(b)|^2][|A''(b)|/|A(b)|] \ll 1$ and $\omega_0{}^2[|\varphi''(b)|/|\varphi'(b)|] \ll 1$ are satisfied. As for the WFT, the instantaneous frequency of the signal can also be extracted from the wavelet ridge,

$$\varphi'(b) = \xi_{rb} = \frac{\omega_0}{a_{rb}}, \tag{18}$$

where a_{rb} denotes the value of a at the instant b on the ridge.

3. One-Dimensional Temporal Analysis of an Interferogram Sequence

After a brief illustration of the above-mentioned three signal processing techniques, their perfor-

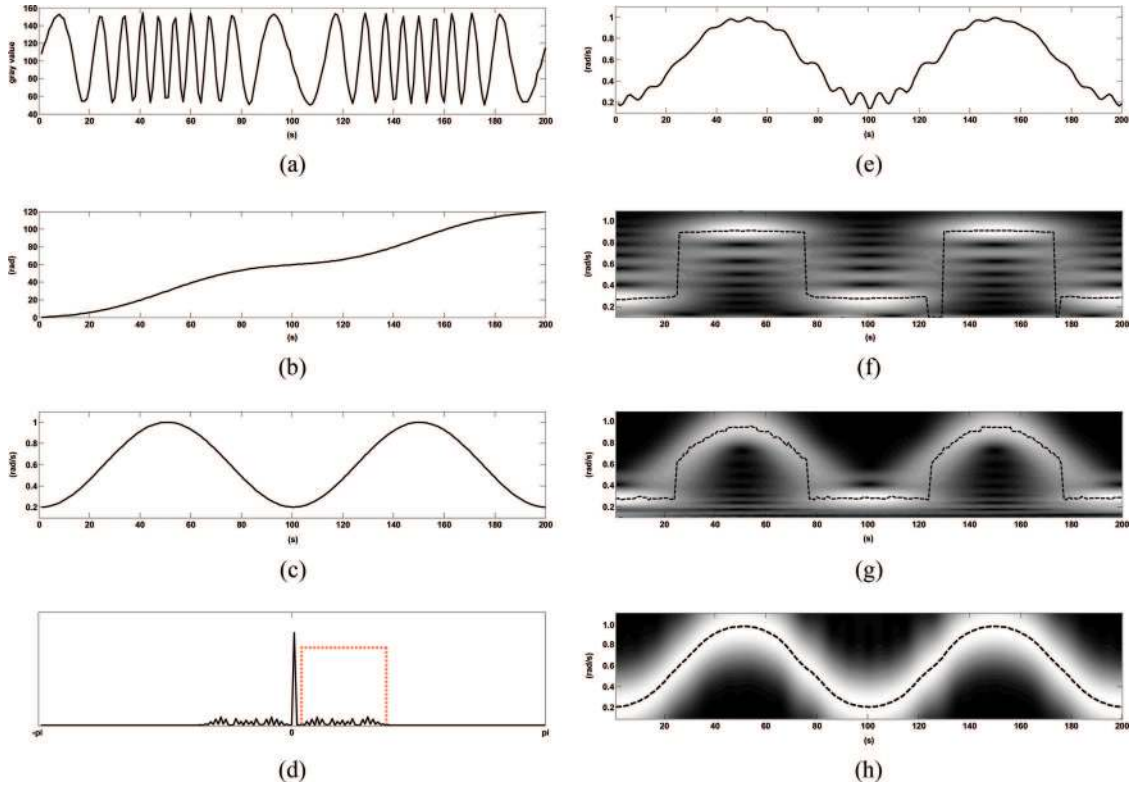

Fig. 2. (Color online) (a) Simulated intensity variation on a vibrating object with a temporal carrier; (b) theoretical phase value of signal in (a); (c) first-order derivative of the phase value; (d) Fourier spectrum of the signal; (e) first-order derivative of the phase obtained by Fourier bandpass filtering and a numerical differentiation; (f) modulus of the WFT when $\sigma = 20$ and the corresponding ridge; (g) modulus of the WT and the corresponding ridge; and (h) ridge obtained by a combination of FFT and WT processing.

mance for the extraction of phase and phase derivatives from signals $f_I(t)$ and $f_{II}(t)$ will be presented, based on simulation and experimental results.

A. Speckle or Fringe Pattern Sequence with Temporal Carrier

In the processing of a real signal where the three terms in Eq. (5) are separable, it is worth noting that:

(1) A FT always gives a reasonable result when a proper filtering window is selected. However, the FT cannot remove the noise whose frequency is superimposed on the signal frequency. Therefore, the accuracy is not very high when the signal frequency band is broad.

(2) In the WFT, the window size σ_t is determined by several factors. (a) In the WFT, the signal phase is assumed to be linear in the area covered by the Gaussian window. However, in temporal analysis it is normal that the frequency varies dramatically. Hence the window size should be small in order to reduce the linear phase approximation error. (b) A larger window size performs better in noise elimination. However, in temporal analysis, the signal is not very noisy even in speckle interferometry as the intensity variation is analyzed pixel by pixel. Normally selecting a large window size is not necessary. (c) A windowed Fourier kernel with a small window size in time will have a large window size in the spectrum. When the low frequency part of the signal is processed, the result will be seriously affected by the *DC* term. Accordingly to our experience, for a certain signal frequency ξ, the window size in time should satisfy $\sigma_t \geq 2.0/\xi$ to avoid the influence of the *DC* term. (d) A compromise between (a) and (b) is not difficult in temporal analysis. However, the conflict between (a) and (c) is inevitable in many cases and will usually cause a large system error. One of the solutions is to remove the *DC* term before the WFT.

(3) In the WT, the influence of the *DC* term can be ignored when $\omega_0 > 5$. However, the WT performs very poorly when the signal frequency is low, as it will automatically adjust the window size σ_t to be very large, sometimes even larger than the signal length. This will generate large errors in the phase extraction. Normally a WT only performs well when the signal frequency is high and has small variation.

Figure 2(a) shows a simulated temporal intensity variation of a vibrating object with a temporal carrier. Some random noise is added to the signal. The noise is set as 5% of the signal amplitude. Figures 2(b) and 2(c) show the theoretical phase value $\varphi(t)$ and its first-order derivative $\varphi'(t)$. Figure 2(d) is the Fourier spectrum of the signal. The dotted line roughly indicates the signal frequency band, which is quite broad. Figure 2(e) shows the first-order derivative of the phase obtained by a Fourier bandpass filtering and a numerical differentiation. The noise effect is still quite obvious in the FT result. Figure 2(f) shows the modulus of the WFT. The dashed curve shows the ridge where the maximum moduli are found. $\sigma = 20$ is selected as a window size to avoid the influence of the *DC* term. However, it is obviously not sensitive enough to the frequency variation. This is

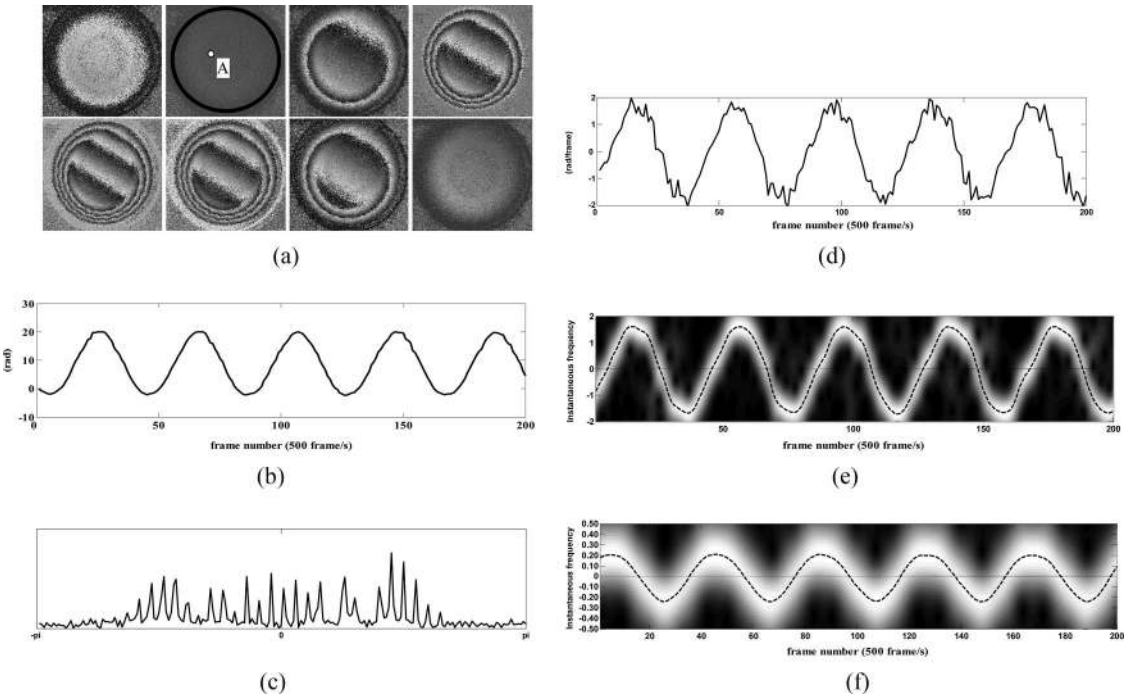

Fig. 3. (a) Some typical wrapped phase maps at different instants obtained by image-plane digital holography; (b) phase variation at point A; (c) spectrum of the exponential phase signal; (d) first-order derivatives of the phase after FT filtering; (e) modulus of the WFT and corresponding ridge; and (f) WFT ridge proportional to the acceleration.

due to the conflict of points (a) and (c) in the WFT process mentioned above. Figure 2(g) shows the wavelet ridge of the signal. The WT performs well in a high-frequency range, but gives incorrect results in the low frequency range. The main problem involved is that the window size σ_t selected automatically by WT is not small enough, so the linear phase approximation error seriously affects the result.

So far FT performs the best in the first-order phase derivative extraction. A new processing technique based on the combination of FT and WFT is suggested here to improve the results. An signal varying in intensity is processed by FT and bandpass filtering so that the negative frequency and *DC* term are removed. The wrapped phase obtained by FT is converted to an exponential phase signal f_{II} and then processed again by a WFT with a small σ_t. Figure 2(h) shows the results from a FT + WFT processing. $\sigma_t = 4$ is selected for the WFT window size. A perfect WFT ridge is obtained this time. From the simulation results shown above, it can be concluded that for a real signal of temporal intensity variation f_{I}, it is better to convert it to an exponential phase signal f_{II} first by a Fourier analysis, and then to process it by WFT.

B. Wrapped Phase Sequence

In the temporal analysis of an exponential phase signal f_{II}, a temporal carrier is not necessary as the phase ambiguity problem does not exist. For a vibrating object, the spectrum of this exponential signal f_{II} will contain values around the zero frequency, with a certain bandwidth from negative to positive frequencies. The width of the spectrum depends on the value of the second-order derivative of the phase, in this case the acceleration. The purpose of the processing is the filtering of the noise and the extraction of the derivatives of the phase, which lead to the measurement of some other useful physical properties. In a windowed Fourier analysis, the conflict of conditions (a) and (c) mentioned above does not exist. Therefore applying a FT analysis before the WFT is not necessary. Due to the poor performance of the WT at low frequency, it is not practical to process the signal when the frequency is approximately zero. Results from the FT and WFT are presented below, based on an experimental result of image-plane digital holography [30,31].

The object measured is the membrane of a Panasonic earphone (Model RP-HV103). A low-frequency signal (~12 Hz) is applied by a function generator. Figure 3(a) shows some typical wrapped phase maps reconstructed from the digital hologram sequence at different instants. Two hundred frames are captured, at an imaging rate of 500 fps, by a Basler A504k camera with a pixel size of 12 μm × 12 μm. Figure 3(b) shows the phase variation of point A [shown in Fig. 3(a)] after temporal unwrapping. The phase has been converted to an exponential signal and its spectrum is shown in Fig. 3(c). Figure 3(d) shows the first-order derivative of the phase after FT filtering. A noise effect is still very obvious due to the broad frequency band of the signal. The modulus of the WFT is shown in Fig. 3(e). The dashed curve shows the ridge where the maximum moduli are found. The window size is selected as $\sigma_t = 3$ due to the large variation of the frequency. Then another exponential signal is calculated by

$$f_{\mathrm{II}}(t) = U(x, y; t_n)U^*(x, y; t_{n-1}) = \exp(j\varphi(x, y; t_n))\exp(-j\varphi(x, y; t_{n-1})), \quad (19)$$

where the phase values are proportional to the numerical differentiation of the displacement. Processing of this signal leads to the evaluation of the acceleration of the object. Figure 3(f) is the WFT ridge, which is proportional to the acceleration. The window size selected this time is $\sigma_t = 5$. The results of the kinematic parameter evaluation on the vibrating membrane are shown in Fig. 4. Figure 4(a) shows a 3D plot of the instantaneous displacement of the membrane at frame 100 ($t = 0.198$ s). It is obtained from 1D temporal windowed Fourier analysis followed by a 5 × 5 median filter to remove some badly

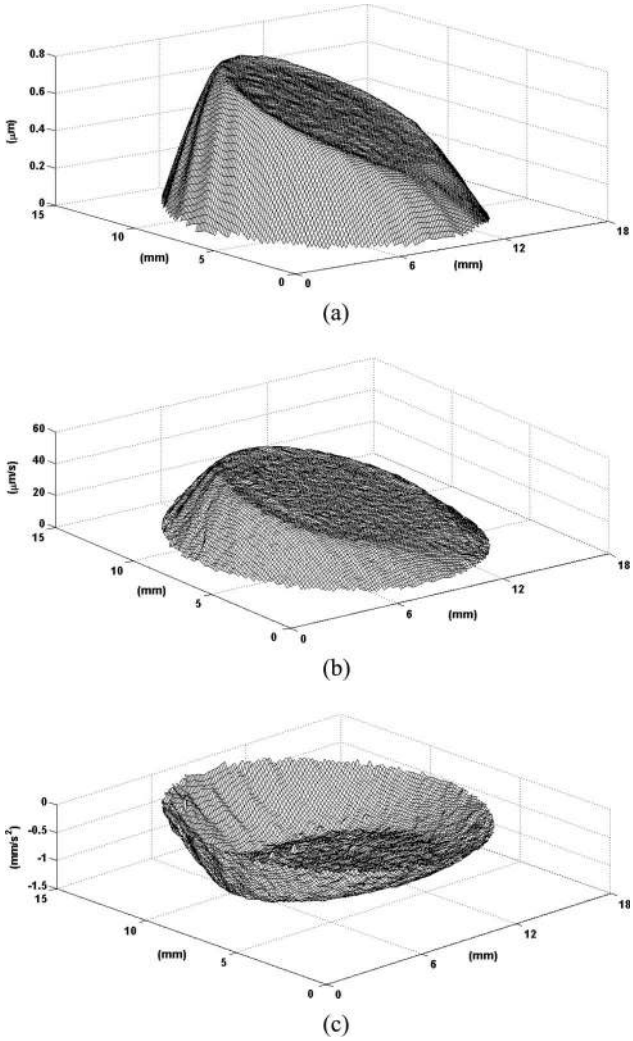

Fig. 4. Three-dimensional plot of the instantaneous (a) displacement, (b) velocity, and (c) acceleration at frame number 100.

behaved pixels. Figures 4(b) and 4(c) are 3D plots of the instantaneous velocity and acceleration at frame 100. A smooth spatial distribution of the displacement, velocity, and acceleration can be obtained at any instant, which presents a good evaluation of the kinematic parameters by the proposed windowed Fourier analysis.

4. Two-Dimensional Analysis

After a temporal analysis on each pixel, the spatial distribution of the phase at any instant can be obtained. If the spatial phase variation is still within the Nyquist frequency, which implies at least two pixels within 2π phase change, the above-mentioned signal processing techniques, especially the WFT can be extended to the 2D case and used to extract the deformation parameters at any instant of a continuously deforming or a vibrating object. It is worth noting that the WT is still not suitable for the 2D exponential phase signal f_{II} due to the poor performance at low frequency.

From the 1D case, we know that a WFT is usually more efficient in noise elimination for exponential phase signal. This conclusion can be extended to the 2D and 3D cases. Some other filtering algorithms, such as the sine–cosine average filter (SCAF) [32], are also available for wrapped phase filtering. SCAF is often used due to its simplicity. However, it is not adaptive to the fringe patterns with spatially varying frequency and can only process the wrapped phase maps with small slopes [33]. Therefore, only a WFT is illustrated here to demonstrate its capability in deformation parameter evaluation.

Figure 5(a) shows a simulated phase map of a fully clamped circular plate under uniform pressure loading. A Gaussian noise with power of 0.1 dB W (decibels with reference to a watt) is added to the phase map. The theoretical first-order phase derivative in the x direction and the numerical differentiation of the simulated noisy signal in cross section B-B [indicated in Fig. 5(a)] are given in Fig. 5(b). The wrapped phase maps are then converted to a 2D exponential phase matrix and processed by a 2D WFT to extract the phase derivatives in the x and y directions. The window size σ_x and σ_y of the WFT kernel in the x and y directions are set to be equal in this study and different window sizes are applied. Figure 5(c) shows a comparison of absolute errors in a $\partial w/\partial x$ evaluation of different window sizes. A small σ is more sensitive to the phase variation but performs poorly in the noise elimination. On the contrary, a larger σ will generate a large error in an area where the phase has a sudden change. However, a proper selection of σ yields an accurate extraction of the surface strains $\partial w/\partial x$ and $\partial w/\partial y$. Similarly ridge extraction from the phase map $\exp(j\varphi(x, y; t))\exp(-j\varphi((x-1), y; t))$ yields the second-order derivatives $\partial^2 w/\partial x^2$ and $\partial^2 w/\partial x \partial y$, which are much more important in stress analysis. Figure 5(d) shows the theoretical value of $\partial^2 w/\partial x^2$ and the results obtained by the WFT with different

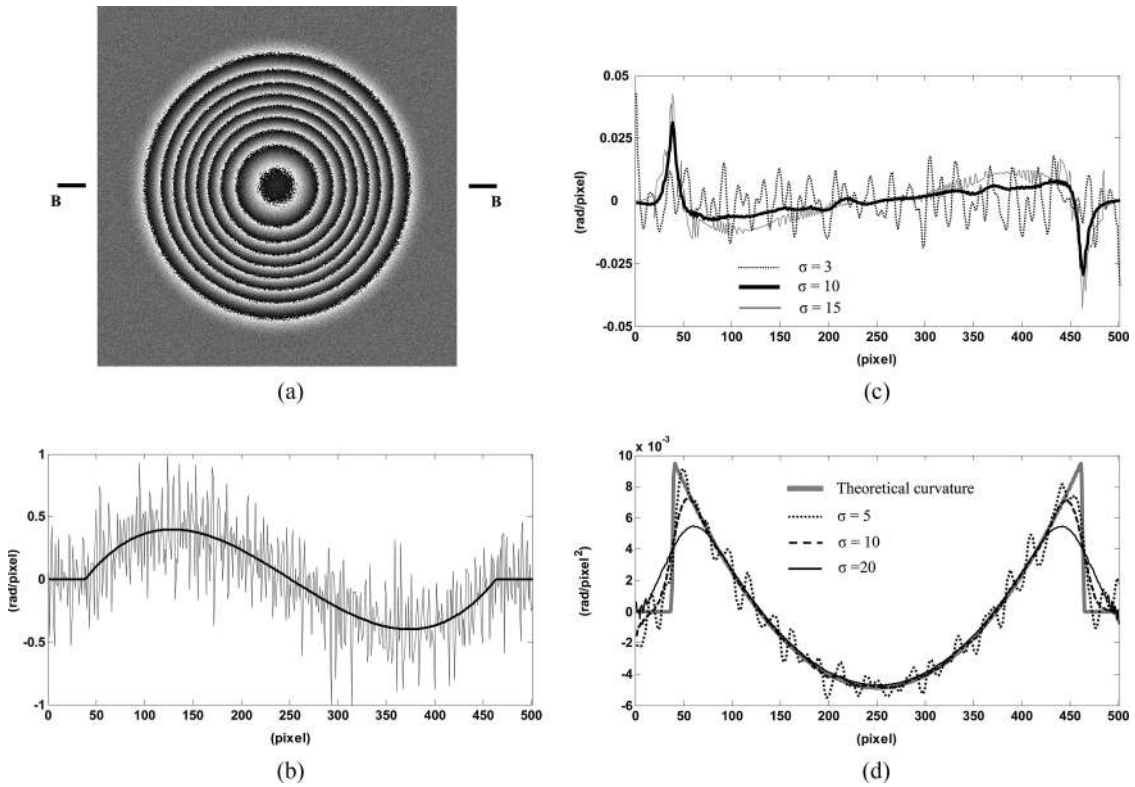

Fig. 5. (a) Simulated wrapped phase map with noise on a fully clamped circular plate, loaded by uniform pressure; (b) theoretical value of dw/dx and simulated noise signal; (c) absolute errors of dw/dx measurement by WFT with different window sizes; and (d) comparison of theoretical curvature value with WFT results using different window sizes.

window sizes. WFT performs well at the center of the plate but poorly at the edge where a discontinuity is observed. However, in a real structure, the errors will not be so large as the curvature and twist are still continuous in many cases. Although it is quite difficult to quantify the error at each pixel in real measurement, the average relative error should be less than 5% for the strain measurement and 10% for the curvature and twist measurements.

Figure 6 shows the deformation parameter evaluation by a WFT on a speckle sequence captured by a high-speed camera in an ESPI setup. The specimen is a fully clamped square plate with several artificial defects (circular blind holes with different depths). The width and thickness of the plate are 80 and 5 mm, respectively. The plate is loaded by a uniformly distributed pressure, applied with compressed air and is continuously deformed by increments of pressure. During the deformation of the object, a series of speckle patterns is captured by a high-speed CCD camera (Kodak motion corder analyzer, SR-Ultra) with an image rate of 250 fps. Three hundred speckle patterns are captured during a 1.2 s period. Figure 6(a) shows a typical ESPI fringe pattern by subtraction of frame 300 from frame 1. Figure 6(b) is a wrapped phase map at instant $t = 1.2$ s obtained by temporal Fourier analysis. Converting it to an exponential phase signal and extracting the WFT ridge yields the evaluation of the surface strains $\partial w/\partial x$ [shown in Fig. 6(c)] and $\partial w/\partial y$ [shown in Fig. 6(d)]. The grayscale map of curvature $\partial^2 w/\partial x^2$ and twist $\partial^2 w/\partial x \partial y$ are shown in Figs. 6(e) and 6(f).

The above example shows 2D WFT processing in the spatial domain after a 1D temporal Fourier analysis. It is worth noting that the WFT can also be applied to the spatiotemporal planes of x–t and y–t. These kinematic and deformation parameters can be obtained from one 2D WFT process. It is more suitable for a measurement on a beam where a 2D spatial distribution of the parameters is not necessary.

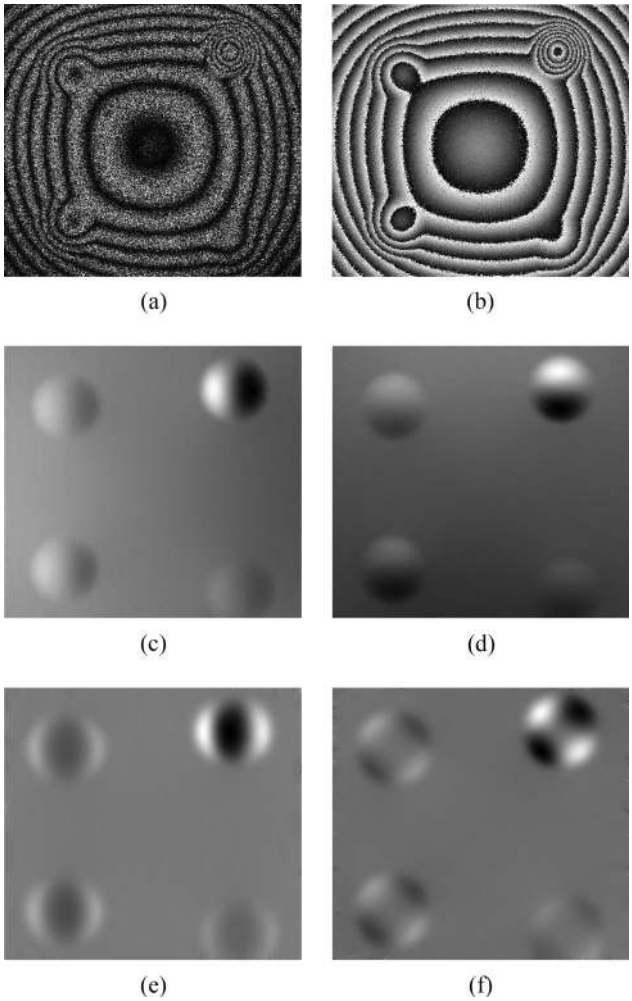

Fig. 6. (a) Typical ESPI fringes at frame 300; (b) wrapped phase map obtained by temporal Fourier analysis at frame 300; (c) grayscale map indicating the instantaneous spatial distribution of dw/dx; (d) grayscale map indicating the instantaneous spatial distribution of dw/dy; (e) grayscale map indicating the instantaneous spatial distribution of curvature d^2w/dx^2; and (f) grayscale map indicating the instantaneous spatial distribution of twist $d^2w/dxdy$.

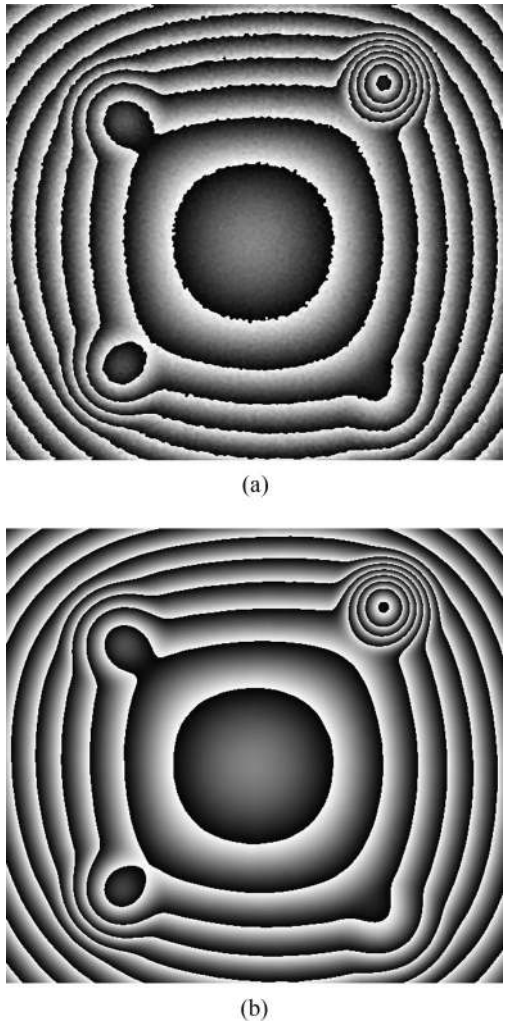

Fig. 7. (a) Wrapped phase obtained by 3D Fourier filtering and (b) wrapped phase obtained by 3D windowed Fourier filtering.

5. Three-Dimensional Spatiotemporal Analysis

The above-mentioned Fourier analysis and windowed Fourier analysis can also be extended to a 3D case. This means a 3D kernel will be used to process a matrix in x–y–t space. A 3D process is only practicable when the Nyquist sampling theorem is satisfied along all three directions. A 3D WFT is not recommended as it normally takes a long processing time and evaluates some parameters that sometimes is not very useful, such as $\partial^2 w/\partial x \partial t$. However, it is more efficient in noise elimination as more sampling points are covered in a 3D kernel, and it also allows more flexibility in selecting the window sizes σ_x, σ_y, and σ_t in order to achieve the compromise between reducing the linear phase approximation error and noise elimination. Figures 7(a) and 7(b) show the wrapped phase map at instant $t = 1.2$ s after the 3D FT and after the 3D WFT. The 3D WFT gives a perfect filtering result on the phase distribution. $\sigma_x = \sigma_y = 5$ and $\sigma_t = 10$ are selected in this study as the nonlinearity of phase is more serious in the x and y directions than in the time axis.

6. Conclusion

In this paper we have presented different processing algorithms for evaluating kinematic and deformation parameters from an interferogram sequence. Temporal analysis is normally the first step in a dynamic optical measurement. For an intensity varying signal, a Fourier analysis is necessary to remove the influence of the *DC* term and to convert the real signal to an exponential phase signal. However, a Fourier analysis cannot remove noise whose frequencies are superimposed with signal frequencies. Windowed Fourier analysis then becomes a typical processing technique to filter the noise and to extract the derivatives of the phase. Instantaneous kinematic parameters, such as displacement, velocity, and acceleration, can be obtained by temporal analysis. The criteria for the selection of window size in WFT were also discussed. A large window size performs better in noise elimination, but generates more error when the signal phase variation is nonlinear. The processing results in the simulations and the experiments show the capability of the WFT in phase and phase derivatives extraction. Compared to the WFT, the application of the WT is limited due to the poor performance in the low-frequency part. Similar situations are found in 2D spatial and 3D spatiotemporal analysis for deformation parameters evaluation when the Nyquist sampling theorem is satisfied along all axes. The proposed algorithms show that it is now possible to have a whole-field, noncontact optical measurement of different useful parameters.

Y. Fu gratefully acknowledges the financial support of the Alexander von Humboldt Foundation. This work is also supported by the German Science Foundation, DFG, grant OS. 111/22-1, the MULTIENCODE project [006427 (SSPI)], funded by the European Union and the National Science Foundation of China (NSFC) under contract 10772171.

References

1. M. Takeda, H. Ina, and S. Kobayashi, "Fourier-transform method of fringe-pattern analysis for computer-based topography and interferometry," J. Opt. Soc. Am. **72,** 156–160 (1982).
2. J. M. Huntley, G. H. Kaufmann, and D. Kerr, "Phase-shifted dynamic speckle pattern interferometry at 1 kHz," Appl. Opt. **38,** 6556–6563 (1999).
3. K. A. Stetson and R. L. Powell, "Interferometric hologram evaluation and real-time vibration analysis of diffuse objects," J. Opt. Soc. Am. **55,** 1694–1695 (1965).
4. S. Nakadate, "Vibration measurement using phase-shifting time-average holographic interferometry," Appl. Opt. **25,** 4155–4161 (1986).
5. D. I. Farrant, G. H. Kaufmann, J. N. Petzing, J. R. Tyrer, B. F. Oreb, and D. Kerr, "Measurement of transient deformations with dual-pulse addition electronic speckle-pattern interferometry," Appl. Opt. **37,** 7259–7267 (1998).
6. S. Schedin, G. Pedrini, H. J. Tiziani, and F. M. Santoyo, "Simultaneous three-dimensional dynamic deformation measurements with pulsed digital holography," Appl. Opt. **38,** 7056–7062 (1999).
7. G. Pedrini, H. Tiziani, and Y. Zou, "Digital double pulse-TV-holography," Opt. Lasers Eng. **26,** 199–219 (1997).
8. http://www.photron.com/content.cfm?n=products&id=SlowMotionVideo.
9. G. Pedrini, W. Osten, and M. E. Gusev, "High-speed digital holographic interferometry for vibration measurement," Appl. Opt. **45,** 3456–3462 (2006).
10. J. M. Huntley and H. Saldner, "Temporal phase-unwrapping algorithm for automated interferogram analysis," Appl. Opt. **32,** 3047–3052 (1993).
11. C. Joenathan, B. Franze, P. Haible, and H. J. Tiziani, "Speckle interferometry with temporal phase evaluation for measuring large-object deformation," Appl. Opt. **37,** 2608–2614 (1998).
12. H. J. Tiziani, "Spectral and temporal phase evaluation for interferometry and speckle applications," in *Trends in Optical Nondestructive Testing and Inspection,* P. K. Rastogi and D. Inaudi, eds. (Elsevier Science B. V., 2000), pp. 323–343.
13. G. H. Kaufmann, "Phase measurement in temporal speckle pattern interferometry using the Fourier transform method with and without a temporal carrier," Opt. Commun. **217,** 141–149 (2003).
14. X. Colonna de Lega, "Processing of non-stationary interference patterns: adapted phase shifting algorithms and wavelet analysis. Application to dynamic deformation measurements by holographic and speckle interferometry," Ph.D. dissertation 1666 (Swiss Federal Institute of Technology, 1997).
15. M. Cherbuliez and P. Jacquot, "Phase computation through wavelet analysis: yesterday and nowadays," in *Fringe 2001,* W. Osten and W. Juptner, eds. (Elsevier, 2001), pp. 154–162.
16. Y. Fu, C. J. Tay, C. Quan, and L. J. Chen, "Temporal wavelet analysis for deformation and velocity measurement in speckle interferometry," Opt. Eng. **43,** 2780–2787 (2004).
17. Y. Fu, C. J. Tay, C. Quan, and H. Miao, "Wavelet analysis of speckle patterns with a temporal carrier," Appl. Opt. **44,** 959–965 (2005).
18. C. J. Tay and Y. Fu, "Determination of curvature and twist by digital shearography and wavelet transform," Opt. Lett. **30,** 2873–2875 (2005).
19. K. Qian, S. H. Seah, and A. Asundi, "Phase-shifting windowed Fourier ridges for determination of phase derivatives," Opt. Lett. **28,** 1657–1659 (2003).
20. K. Qian, "Windowed Fourier transform for fringe pattern analysis," Appl. Opt. **43,** 2695–2702 (2004).

21. K. Qian, "Two-dimensional windowed Fourier transform for fringe pattern analysis: principles, applications and implementations," Opt. Lasers Eng. **45,** 304–317 (2007).
22. J. Zhong and J. Weng, "Phase retrieval of optical fringe patterns from the ridge of a wavelet transform," Opt. Lett. **30,** 2560–2562 (2005).
23. A. Federico and G. H. Kaufmann, "Evaluation of the continuous wavelet transform method for the phase measurement of electronic speckle pattern interferometry fringes," Opt. Eng. **41,** 3209–3216 (2002).
24. L. R. Watkins, S. M. Tan, and T. H. Barnes, "Determination of interferometer phase distributions by use of wavelets," Opt. Lett. **24,** 905–907 (1999).
25. K. Qian and H. S. Seah, "Two-dimensional windowed Fourier frames for noise reduction in fringe pattern analysis," Opt. Eng. **44,** 075601 (2005).
26. K. Qian, Y. Fu, Q. Liu, H. S. Seah, and A. Asundi, "Generalized three-dimensional windowed Fourier transform for fringe analysis," Opt. Lett. **31,** 2121–2123 (2006).
27. X. Colonna de Lega and P. Jacquot, "Interferometric deformation measurement using object induced dynamic phase shifting," in *Optical Inspection and Micromeasurements,* C. Goreuki, ed., Proc. SPIE **2782,** 169–179 (1996).
28. X. Colonna de Lege and P. Jacquot, "Deformation measurement with object-induced dynamic phase shifting," Appl. Opt. **35,** 5115–5121 (1996).
29. S. Mallat, *A Wavelet Tour of Signal Processing* (Academic, 1998).
30. J. W. Goodman and R. W. Lawrence, "Digital image formation from electronically detected holograms," Appl. Phys. Lett. **11,** 77–79 (1967).
31. Y. Fu, G. Pedrini, and W. Osten, "Vibration measurement by temporal Fourier analyses of digital hologram sequence," Appl. Opt. **46,** 5719–5727 (2007).
32. H. A. Aebischer and S. Waldner, "A simple and effective method for filtering speckle-interferometric phase fringe patterns," Opt. Commun. **162,** 205–210 (1999).
33. K. Qian, T. H. N. Le, F. Lin, and H. S. Seah, "Comparative analysis on some filters for wrapped phase maps," Appl. Opt. **46,** 7412–7418 (2007).